ACS APPLIED MATERIALS & INTERFACES

Subscriber access provided by King Abdullah University of Science and Technology Library

Article

High-Efficiency InGaN/GaN Quantum Well-Based Vertical Light-Emitting Diodes Fabricated on #-GaO Substrate

Mufasila Muhammed, Norah Alwadai, Sergei Lopatin, Akito Kuramata, and Iman S Roqan

ACS Appl. Mater. Interfaces, **Just Accepted Manuscript** • DOI: 10.1021/acsami.7b09584 • Publication Date (Web): 11 Sep 2017

Downloaded from http://pubs.acs.org on September 17, 2017

Just Accepted

"Just Accepted" manuscripts have been peer-reviewed and accepted for publication. They are posted online prior to technical editing, formatting for publication and author proofing. The American Chemical Society provides "Just Accepted" as a free service to the research community to expedite the dissemination of scientific material as soon as possible after acceptance. "Just Accepted" manuscripts appear in full in PDF format accompanied by an HTML abstract. "Just Accepted" manuscripts have been fully peer reviewed, but should not be considered the official version of record. They are accessible to all readers and citable by the Digital Object Identifier (DOI®). "Just Accepted" is an optional service offered to authors. Therefore, the "Just Accepted" Web site may not include all articles that will be published in the journal. After a manuscript is technically edited and formatted, it will be removed from the "Just Accepted" Web site and published as an ASAP article. Note that technical editing may introduce minor changes to the manuscript text and/or graphics which could affect content, and all legal disclaimers and ethical guidelines that apply to the journal pertain. ACS cannot be held responsible for errors or consequences arising from the use of information contained in these "Just Accepted" manuscripts.

ACS Publications

ACS Applied Materials & Interfaces is published by the American Chemical Society. 1155 Sixteenth Street N.W., Washington, DC 20036
Published by American Chemical Society. Copyright © American Chemical Society. However, no copyright claim is made to original U.S. Government works, or works produced by employees of any Commonwealth realm Crown government in the course of their duties.

High-Efficiency InGaN/GaN Quantum Well-Based Vertical Light-Emitting Diodes Fabricated on β-Ga_2O_3 Substrate

Mufasila M. Muhammed[1], *Norah Alwadai*[1], *Sergei Lopatin*[2], *Akito Kuramata*[3] *and Iman S. Roqan*[1]*.

[1] King Abdullah University of Science and Technology (KAUST), Physical Sciences and Engineering Division, Thuwal 23955-6900, Saudi Arabia.

[2]King Abdullah University of Science and Technology (KAUST), Imaging and Characterization Core Lab, Thuwal 23955-6900, Saudi Arabia

[3]Tamura Corporation and Novel Crystal Technology, Inc., Sayama, Saitama 350-1328, Japan

KEYWORDS: Vertical light emitting diode, electroluminescence, time-resolved photoluminescence, Gallium oxide, scanning transmission electron microscopy.

We demonstrate a state-of-the-art high-efficiency GaN-based vertical light-emitting diode (VLED) grown on a transparent and conductive (-201)-oriented (β-Ga_2O_3) substrate, obtained using a straightforward growth process that does not require a high cost lift-off technique or complex fabrication process. The high-resolution scanning transmission electron microscopy (STEM) images confirm that we produced high quality upper layers, including a multi-quantum well (MQW) grown on the masked β-Ga_2O_3 substrate. STEM imaging also shows a well-defined MQW without InN diffusion into the barrier. Electroluminescence (EL) measurements at room temperature indicate that we achieved a very high internal quantum efficiency (IQE) of 78%; at lower temperatures, IQE reaches ~ 86%. The photoluminescence (PL) and time-resolved PL

analysis indicate that, at a high carrier injection density, the emission is dominated by radiative recombination with a negligible Auger effect; no quantum-confined Stark effect is observed. At low temperatures, no efficiency droop is observed at a high carrier injection density, indicating the superior VLED structure obtained without lift-off processing, which is cost-effective for large-scale devices.

1
2
3
4
5
6
7
8
9
10
11
12
13
14
15
16
17
18
19
20
21
22
23
24
25
26
27
28
29
30
31
32
33
34
35
36
37
38
39
40
41
42
43
44
45
46
47
48
49
50
51
52
53
54
55
56
57
58
59
60

INTRODUCTION

High-efficiency solid-state lighting and high-power electronics are considered among the significant innovations. Materials based on III-nitride are commonly used for these purposes and have attracted the considerable attention of researchers and experts due to their distinct and highly favorable properties, which include a wide direct bandgap, high chemical and thermal stability, and high mobility.[1, 2] These highly desirable characteristics led to high-efficiency devices, such as light-emitting diodes (LEDs) and high-power electronic systems.[2, 3] Vertical-injection GaN-based light-emitting diodes (VLEDs) are of particular importance in this context, as they are promising candidates for high-efficiency and high-power devices.[4, 6] VLEDs provide numerous advantages over the conventional, lateral-injection LEDs, such as better current injection, excellent heat dissipation, enhanced electrostatic discharge, good chip-size scalability, and a simple packaging process.[5] However, the fabrication of current VLED designs is very costly as the process is very complex; the insulating sapphire substrate must be removed by wafer bonding and a lift-off process to achieve the vertical injection, after which the obtained VLED structure must be transferred to a conducting carrier substrate. Furthermore, this transfer process may cause damage to the GaN surface layers, resulting in structural defects and cracks in the epitaxial layers that degrade device performance.[7, 8] When producing VLEDs, SiC or GaN can also be used as the substrate. However, large-scale SiC production is challenging due to the micropipes introduced during the growth process. Moreover, the cost of manufacturing conductive n-doped SiC substrates is prohibitively high, and the resulting material is not transparent, limiting its use in UV LEDs.[9] Similarly, GaN native substrate is commercially unviable, being even more expensive than SiC substrates, and its absorption limitations render it unsuitable for deep UV AlGaN LEDs.[10, 11] Therefore, additional effort is required to increase

1
2
3
4
5
6
7
8
9
10
11
12
13
14
15
16
17
18
19
20
21
22
23
24
25
26
27
28
29
30
31
32
33
34
35
36
37
38
39
40
41
42
43
44
45
46
47
48
49
50
51
52
53
54
55
56
57
58
59
60

GaN production volume and decrease the effective cost per wafer. Similarly, a straightforward and cost-effective VLED manufacturing process is needed to meet the commercial objectives.

Here, we introduce a high-efficiency, GaN-based VLED grown on a transparent and conductive (β-Ga_2O_3) substrate using a cost-effective simple and direct growth process, without the need for a costly lift-off technique or otherwise complicated fabrication process. The β-Ga_2O_3 growth process is not only cost-effective,[12, 13] but the substrate transparency also improves the efficiency of light extraction compared to a GaN substrate, even in UV AlGaN LEDs. In addition, its conductivity assists in mitigating heat and current distribution issues, and permits vertical current injection. The (-201)-oriented β-Ga_2O_3 substrate has a direct wide band gap (4.8 eV) in the UV and visible regions, and shows a much lower lattice mismatch (~ 4.7%) with GaN than has been previously reported in sapphire substrate.[14, 15] A low threading dislocation (TD) density has been demonstrated in wafers grown on such substrates, contributing to the superior GaN quality.[15] These advantages make (-201)-oriented β-Ga_2O_3 substrate an excellent candidate for high optical and structural quality III-nitride material growth, and for addressing the current crowding problems in high-power VLEDs. It also allows integration of multiple cells of smaller size into large-scale VLED chips at a much lower cost than that associated with current substrate processing techniques.

In this work, we demonstrate the superior performance of a state-of-the-art InGaN/GaN multi-quantum well (MQW) VLED grown on (-201)-oriented β-Ga_2O_3 substrate using a direct growth process of metal organic chemical vapor deposition (MOCVD), that eliminates the need for a complicated lift-off and structure-transfer process. We also show that InGaN MQW-based VLEDs exhibit high optical efficiency. Finally, an optical characterization confirms that the

1
2
3
4
5
6
7
8
9
10
11
12
13
14
15
16
17
18
19
20
21
22
23
24
25
26
27
28
29
30
31
32
33
34
35
36
37
38
39
40
41
42
43
44
45
46
47
48
49
50
51
52
53
54
55
56
57
58
59
60

superior optical quality of the LED structures is dominated by radiative carrier injection, accompanied by negligible Auger recombination.

EXPERIMENTAL PROCEDURE

Sample Growth: $In_xGa_{1-x}N$/GaN MQW-based blue VLED was grown by MOCVD on (-201)-oriented monoclinic β-Ga_2O_3 (680 μm thickness) (by Tamura Co and Novel Crystal Technology, Inc). The nominal InN composition was x = 0.15. The substrate was doped with Sn to increase its n-type conductivity, and the carrier density of 10^{18} cm^{-3} was estimated via Hall measurements. The β-Ga_2O_3 substrate was masked with patterned SiN_x arrays (made by standard photolithography patterning and etching). A low-temperature (LT) undoped AlN buffer layer was grown on (-201)-oriented β-Ga_2O_3 substrates using a low-pressure, vertical MOCVD reactor to protect the Ga_2O_3 surface from being nitridized and to supply growth nuclei for the upper GaN layer. The AlN layer thickness was optimized to ∼2 nm to provide good conductivity at the interface and to reduce the lattice mismatch between the substrate and GaN. Then, NH_3 and H_2 carrier gasses were used to grow an n-type Si-doped GaN epilayer (with 4×10^{18} cm^{-3} carrier density and ~ 2.5 μm nominal thickness) at the substrate temperature of 920 °C. To improve the quality of the uppermost GaN layer, the temperature was increased further to 1080 °C, and a second (~ 2.5 μm thick) Si-doped GaN layer was deposited (This two-temperature growth process decreases the formation of epicracks and reduces dislocations, thus improving the quality of the upper n-GaN layer[15]), followed by a pre-MQW InGaN/GaN superlattice (SLS) layer, the $In_xGa_{1-x}N$/GaN MQW structure, and the p-GaN layer (doped with Mg)[16]. During the MQW growth, precursors of trimethylgallium (TMGa), trimethylindium (TMIn), and NH_3 were used as source gasses, while N_2 served as the carrier gas. Figure 1a shows the basic structure of the VLED produced by the aforementioned process.

1
2
3
4
5
6
7
8
9
10
11
12
13
14
15
16
17
18
19
20
21
22
23
24
25
26
27
28
29
30
31
32
33
34
35
36
37
38
39
40
41
42
43
44
45
46
47
48
49
50
51
52
53
54
55
56
57
58
59
60

Structural Characterizations: Cross-sectional specimens were prepared for scanning transmission electron microscopy (STEM), and energy dispersive X-ray (EDX) analysis using a lamellar lift-off procedure on an FEI Helios focused ion beam system. Z-contrast STEM imaging and EDX elemental mapping at 200 kV were performed by a Titan Themis Z 40-300 TEM from Thermo Fisher, USA, equipped with a Super-X EDX detector. To obtain the Z-contrast images, we used a Fischione high-angle annular dark-field detector under the following conditions: 20 mrad probe semi-convergence angle, 100 mm camera length, and 150 pA probe current.

Optical Characterizations: Temperature-dependent photoluminescence (PL) measurements were performed to investigate the luminescence properties of the InGaN/GaN MQW VLED structure using a 325 nm CW He-Cd laser at the 4−300 K temperature range. The excitation laser power was measured at ~ 6 mW; the laser diameter was ~ 100 μm. The spectra were collected by an Andor monochromator attached to a charge coupled device camera. Power-dependent PL (PDPL) and time-resolved PL (TRPL) experiments were conducted using second harmonic (λ = 400 nm) pulses of a mode-locked Ti:sapphire femtosecond pulsed laser (frequency doubled with a barium borate crystal) with a pulse width of ~ 190 fs. The pulse power density was 70 kW/cm^2 with a 2 MHz repetition rate, whereas the power-dependent PL measurements were acquired at a 76 MHz repetition rate. A Coherent Verdi-V18 diode-pumped solid-state CW laser was used to pump the Ti:sapphire laser. In both experiments, the sample emission was detected by a monochromator attached to a UV-sensitive Hamamatsu model C6860 streak camera with a temporal resolution of 10 ps. The samples were mounted on a closed-cycle helium cryostat for all optical measurements.

Electrical Characterizations: The current-voltage (I−V) and electroluminescence (EL) measurements at room temperature (RT) were carried out on the LED chips using a probe station

1
2
3
4
5
6
7
8
9
10
11
12
13
14
15
16
17
18
19
20
21
22
23
24
25
26
27
28
29
30
31
32
33
34
35
36
37
38
39
40
41
42
43
44
45
46
47
48
49
50
51
52
53
54
55
56
57
58
59
60

system (vertical injection). The EL spectra were collected by a near-UV microscope objective (20×) with a numerical aperture of 0.04, linked to the same TRPL detection system.

RESULTS AND DISCUSSION

The structure of the VLED (schematic shown in Figure 1a), allows light to be emitted through the n-GaN and substrate layers using p-contact (Ag/Au/Ti/Au) as a reflective mirror, which helps to increase the light extraction efficiency (LEE) of the VLED.[17] In addition, the heat generation can be minimized compared to lateral injection LED, due to the vertical current distribution and high conductivity of the substrate.[5, 18] We analyzed the structural quality of the InGaN/GaN MQW VLED using high-resolution imaging with STEM in combination with spatially resolved EDX spectroscopy. The cross-sectional Z-contrast (sensitive to atomic number) STEM micrographs of different regions in the VLED epitaxial layers are depicted in Figure 1b-1e, starting with the interface at the β-Ga_2O_3 substrate. Figure 1b shows the interface between the substrate and the n-GaN layer, revealing the patterned SiN_x structures on β-Ga_2O_3 with low-temperature (LT)-grown AlN buffer layer (2 nm). The SiN_x pattern has a lower width of 1.5 μm and a height of 0.8 μm, with a structure-array pitch spacing of 3.5 μm. The SiN_x patterns were employed to (i) improve the crystalline quality of the upper epitaxial layers by reducing the TD penetration to the active region; (ii) improve the light extraction of the VLED devices by avoiding unfavorable reflections in the substrate (the SiN_x refractive index was adjusted to match that of β-Ga_2O_3 (1.9)); and (iii) as the resistivity through the GaN on β-Ga_2O_3 showed a Schottky-like behavior, introducing SiN_x mask improves the resistivity to ohmic-like behavior.[19] An enlarged image of the interface in Figure 1c, captured close to the [100] zone axis by exciting the (0002) Bragg reflection, shows a very low TD density compared to that of high quality LEDs grown on sapphire,[20] and the TDs are terminated within 500 nm of the interface.

1
2
3
4
5
6
7
8
9
10
11
12
13
14
15
16
17
18
19
20
21
22
23
24
25
26
27
28
29
30
31
32
33
34
35
36
37
38
39
40
41
42
43
44
45
46
47
48
49
50
51
52
53
54
55
56
57
58
59
60

This termination of the TDs is explained elsewhere.[20] Figure 1d displays the STEM image of 12 pairs of InGaN QWs/GaN barriers MQWs and 25 underlying pairs of InGaN (1 nm)/GaN (2 nm) pre-MQW SLS layers. The SLS layer assists in spreading the current, further enhancing the device efficiency (including wall-plug efficiency) and improving the VLED performance.[21] Figure 1e shows the atomic-resolution STEM images of the quantum wells (QWs) and the quantum barriers (QBs), revealing a homogeneous thickness (2.5 nm and 6 nm, respectively) and well-defined edges. No TDs are observed in the MQW region. The image of the QW is shown in Figure 1f, where no InN diffusion from the QW to the barrier region is observed, indicating a superior quality, as shown in the EDX Ga and In mapping (Figure 1(g-i)). In addition, no structural defects or inhomogeneous stresses are observed in the QW area, as indicated by the STEM image included in Figure 1f.

Figure 2a shows the I–V curves corresponding to the electrical characteristics of our VLED. The VLED shows a rectifying behavior, with a turn-on voltage of approximately 2.8 V, and a reverse-bias leakage current is absent at voltages below -10 V. The reduction of reverse leakage current noted at a high reverse voltage in InGaN VLEDs is attributed to the high quality of the epitaxial material, with a very low TD density and a low leakage current due to the tunneling effect.[22] The forward voltage at an injection current of 20 mA is 3.7 V, and a bright and uniform light emission is observed over the entire VLED surface (shown in the inset of Figure 2a). These findings, when interpreted jointly, indicate that β-Ga_2O_3 provides uniform current spreading, low resistance, and excellent heat dissipation, which result in reliable high-performance VLED devices.

ACS Paragon Plus Environment

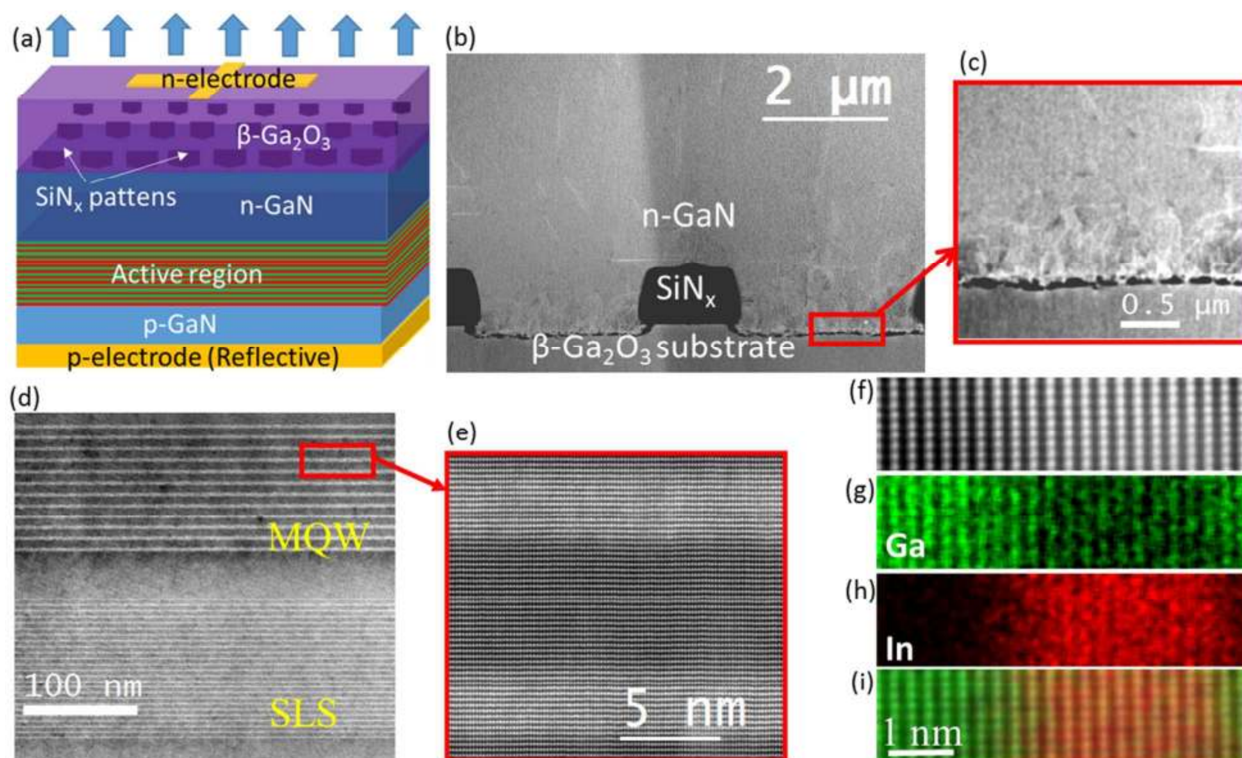

Figure 1. (a) The schematic structure of InGaN/GaN MQW VLED. (b) Cross-sectional STEM image of the interface between the substrate and VLED (The gap at the GaN/β-Ga_2O_3 interface was introduced during the TEM lamella preparation due to the easy cleavage planes of β-Ga_2O_3 substrate that can be damaged during preparation). (c) Enlarged image of the interface indicating the TD density. (d) STEM image of the InGaN/GaN SLS and MQW regions. (e) Atomic resolution STEM image of the QW and QB. (f) STEM image and corresponding EDX elemental map of Ga (g) and In (h), and (i) the superposition of Ga and In map with STEM image.

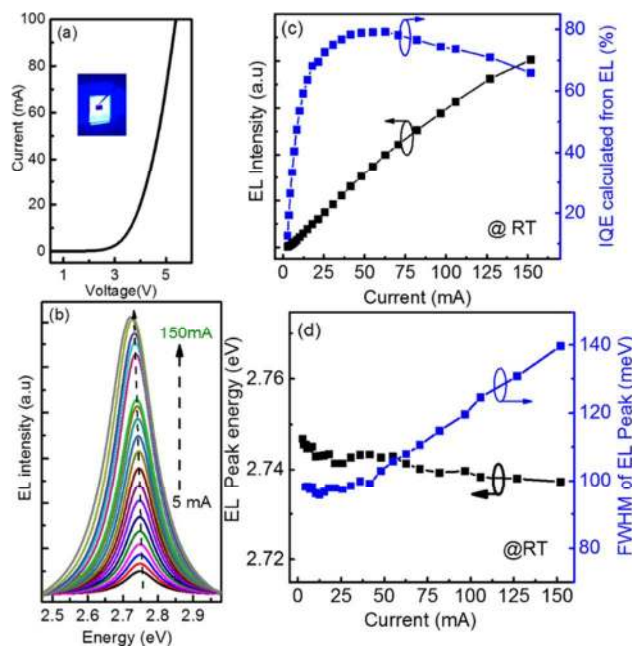

Figure 2. (a) I−V curve from InGaN/GaN MQWs VLED grown on β-Ga_2O_3 substrate (image of EL emission at an injection current of 20 mA is shown in the inset). (b) EL spectra as a function of the injection current in the VLED. (c) EL intensity and IQE as functions of the injection current for the VLED. (d) EL peak energy (black) and FWHM (blue) vs. the injection current.

To assess the efficiency of the VLED, we investigate device efficiency and EL measurements (at RT) as a function of the carrier generation rate. LED efficiency is typically evaluated in terms of the external quantum efficiency (EQE), the internal quantum efficiency (IQE), and the LEE. A decrease in EQE with an increase in the injection current is normally ascribed to a reduction in IQE, since LEE is usually constant, regardless of changes in the injection current.[23] Thus, when investigating the VLED efficiency and droop, IQE is the most important factor.[24] Figure 2b shows the EL spectra of the InGaN/GaN MQW VLED as the input current increases from 2 mA to 150 mA. At an injection current of 20 mA, a strong and sharp blue emission peak with a 97 meV full width at half maximum (FWHM) appears at ~ 452 nm. Figure 2c shows the EL peak intensity and the calculated IQE as functions of the input current.

1
2
3
4
5
6
7
8
9
10
11
12
13
14
15
16
17
18
19
20
21
22
23
24
25
26
27
28
29
30
31
32
33
34
35
36
37
38
39
40
41
42
43
44
45
46
47
48
49
50
51
52
53
54
55
56
57
58
59
60

The IQE values were extracted from the EL data by applying the simplified ABC rate equation to fit the experimental EL data.[25, 26] According to this model, the IQE and the different contributions from the radiative and non-radiative recombination processes at specific injection currents can be calculated without first obtaining the exact values of the A, B, and C coefficients. The rate equation of G (the total carrier generation rate) can be written as [25, 27]

$$G = An + Bn^2 + Cn^3 , \tag{1}$$

where An represents the Shockley-Read-Hall (SRH) non-radiative recombination rate, Bn^2 is the radiative recombination rate, and Cn^3 is the Auger-like or carrier overflow non-radiative recombination rate. Moreover, the integrated EL intensity (I_{EL}) is proportional to the radiative recombination rate (Bn^2) in the QW. By replacing n with I_{EL} in Equation 1 and rewriting the electrical carrier generation (G_{ele}) in terms of the applied current (I) (the derivation is shown in the Supporting Information), and using the fitting parameters (P_2) (Supporting Information Equation S4), the IQE can be deduced as

$$\eta_{IQE} = \frac{Bn^2}{G_{ele}} = \frac{I_{EL}P_2}{I}. \tag{2}$$

As shown in Figure 2c, the EL output intensity increases as the applied current increases. The maximum η_{IQE} value (~ 78%) is observed at an injection current of 33 mA. The efficiency droop (~ 17%) is calculated by comparing this maximum IQE value, and that measured at 160 mA. No decline in the EL intensity is observed in this injection range, indicating a good performance of the device and suggesting that the Auger recombination is negligible at high carrier injection rates. Therefore, the IQE droop can be ascribed to the saturation of the non-radiative recombination rate at low currents, and an increase in the SRH process of the non-radiative recombination rates at high currents.[28]

1
2
3
4
5
6
7
8
9
10
11
12
13
14
15
16
17
18
19
20
21
22
23
24
25
26
27
28
29
30
31
32
33
34
35
36
37
38
39
40
41
42
43
44
45
46
47
48
49
50
51
52
53
54
55
56
57
58
59
60

To further investigate the cause of the droop noted in our VLED, we studied the peak energy and the FWHM of the EL peak as a function of the input current. Figure 2d shows that, as the current increases from 50 mA to 160 mA, the peak energy remains relatively constant, with a very slight redshift (~ 8 meV). On the other hand, while the FWHM remains constant at low current values (up to 45 mA), it increases at higher current values. The behavior of the FWHM and the position of the peak at low current injection values can be attributed to a negligible quantum-confined Stark effect (QCSE) caused by the very small piezoelectric internal electric field and a few localized energy states in the MQWs. The abatement of this piezoelectric field can be attributed to the high quality of the GaN upper layers, which are characterized by reduced strain and dislocation densities at the QW/QB interface grown on (-201)-oriented monoclinic β-Ga_2O_3.[14-15] Thus, the increase in the FWHM and the slight red-shift of the emission peak can be ascribed to the known band filling of the low energy band tail by carriers in the QWs in the high injection carrier density region[29] and to the effect of bandgap renormalization from the enhanced indium composition inside the QWs.[30]

The temperature-dependent PL (TDPL) measurements were carried out to elucidate the thermal activation of the carriers from the QWs and QBs at different temperatures. For this purpose, λ = 325 nm (above the QB bandgap) laser excitation was chosen, as the EL measurements were carried out by exciting the carriers from both the QWs and QBs. Figure 3a shows the integrated intensity as a function of temperature (the PL spectra of the MQWs at RT and 4 K are presented in the inset); the peak intensity initially decreases with the increase in temperature, after which it remains constant. This plateau is observed at temperatures up to 170 K, indicating the high quality of the active region and the low defect densities, as the activation of non-radiative recombination centers occurs at higher temperatures (> 170 K),[31] causing

thermal quenching of the PL intensity. Figure 3b shows the temperature dependence of both the PL peak energy and the FWHM. The PL peak energy as a function of temperature exhibits a slight "S-shape" behavior.[32] The FWHM, however, remains constant (with a negligible increase) up to 190 K, after which a gradual increase is observed. This increase is attributed to the band filling of the localized states, reinforcing the IQE behavior revealed by the EL measurements.

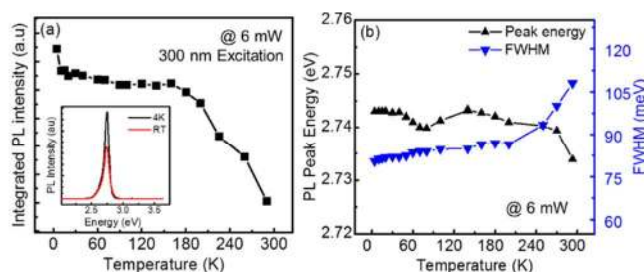

Figure 3. Temperature-dependent integrated PL analysis of the VLED structures under 325 nm laser excitation at 6 mW power. (a) Integrated PL intensity as a function of temperature increase (from 4 K to RT). The inset shows the PL spectra of the MQW peak at 5 K and RT (the ratio of the PL intensity at RT to that at 5 K is 72.5%). (b) PL peak position and FWHM of the MQW peak as a function of temperature.

To investigate the carrier dynamics of the active region inside the QWs, PDPL studies were performed using above-bandgap excitation (400 nm) to excite the carriers generated inside the InGaN QWs only. Selective excitation avoids optical carrier generation in the QBs. As the excitation power increases, the optically generated carriers can be expressed in terms of G_{opt}, as described in Equation 1. Here, if the carrier recombination is dominated by the radiative process, in Equation 1, $An \ll Bn^2$. In other words, the PL intensity I_{PL} is proportional to both G_{opt} and the power density (with a slope of ~ 1 in a log-log plot of power density and I_{PL}), demonstrating that the recombination is dominated by radiative transitions. When the process is dominated by

1
2
3
4
5
6
7
8
9
10
11
12
13
14
15
16
17
18
19
20
21
22
23
24
25
26
27
28
29
30
31
32
33
34
35
36
37
38
39
40
41
42
43
44
45
46
47
48
49
50
51
52
53
54
55
56
57
58
59
60

non-radiative recombination, $Bn^2 \ll An$ and I_{PL} is proportional to $(G_{opt})^2$ (a slope of $\sim$ 2), demonstrating that a non-radiative recombination process is dominant.[25, 33] Figure 4a shows the integrated PL intensity (I_{PL}) as a function of the excitation power density for the VLED structure at RT. Under a low excitation power density, a superlinear dependence of I_{PL} on the excitation power density is observed, whereby the slope of $\sim$ 1.46 indicates that the defect-related non-radiative recombination contributes to the total recombination process. However, as the injected carrier density increases, the non-radiative centers become saturated, resulting in a gradual increase in the radiative recombination, which is consistent with the findings yielded by the EL measurements. At high carrier densities ($\geq 10\times10^3$ kW/cm^2), the radiative recombination dominates the recombination process completely (a slope of $\sim$1 in Figure 4a), resulting in a noticeable increase in the IQE. Furthermore, at high density carrier injection, our VLED did not show Cn^3 behavior indicated by the ABC rate equation (Equation 1), implying that Auger recombination is insignificant. Surprisingly, at 5 K, the slope of the log-log plot is $\sim$1 regardless of the excitation density, as shown in the inset of Figure 4a. This finding demonstrates that the non-radiative centers are quenched at low temperatures, and the radiative recombination dominated the process at all injected carrier densities. Figure 4b shows that the PL peak energy and the corresponding FWHM remained roughly constant at RT as the carrier density increases to 50×10^3 kW/cm^2 and 2×10^3 kW/cm^2, respectively, indicating a negligible QCSE and confirming our EL results. When the excitation density increases further ($> 10\times10^3$ kW/cm^2), the FWHM gradually increases due to the contribution of the band-filling effect of the high-energy localized centers, [27, 29]resulting in a peak blue-shift above 50×10^3 kW/cm^2.

1
2
3
4
5
6
7
8
9
10
11
12
13
14
15
16
17
18
19
20
21
22
23
24
25
26
27
28
29
30
31
32
33
34
35
36
37
38
39
40
41
42
43
44
45
46
47
48
49
50
51
52
53
54
55
56
57
58
59
60

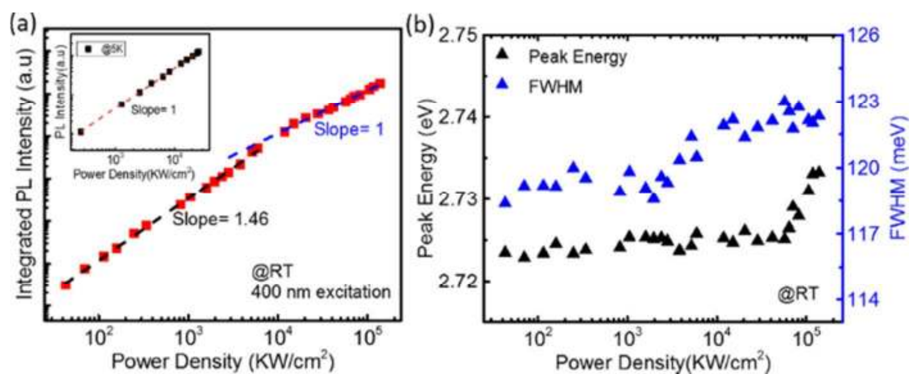

Figure 4. (a) Log-log plot of the integrated PL intensity output vs. the optically injected power density at RT. The values are fitted using two different slopes; the inset shows the same relationship at 5 K. (b) Analysis of the peak energy and FWHM of PDPL MQW emission spectra as a function of optically injected power density at RT.

The IQE is calculated from the PDPL measurements using the ABC model (Equation S1, generated in terms of the optically generated carriers (G_{opt}) in the Supporting Information); by using the fitting parameter (Q_2) (Supporting Information Equation S7), the IQE can be expressed as [25]

$$\eta_{IQE} = \frac{Bn^2}{G_{opt}} = \frac{Q_2 I_{PL}}{G_{opt}}. \quad (3)$$

This optical IQE behavior cannot be directly compared with the device IQE discussed earlier, which was calculated from the EL measurements, since the excitation method is completely different. Figure 5a shows the power-dependent IQE inside the QWs only (at 400 nm excitation) as a function of power density (corresponding to the generated carrier density) at 5 K and RT. At 5 K and under a lower excitation density (< 5×10^3 kW/cm^2) the IQE values remain constant, which indicates that the non-radiative recombination centers were almost inactive, as shown in Figure 5a. At 5 K and under a higher excitation density (> 5×10^3 kW/cm^2), the IQE increases until it reaches a maximum of ~ 86% at ~ 6.3×10^3 kW/cm^2, which is followed by

1
2
3
4
5
6
7
8
9
10
11
12
13
14
15
16
17
18
19
20
21
22
23
24
25
26
27
28
29
30
31
32
33
34
35
36
37
38
39
40
41
42
43
44
45
46
47
48
49
50
51
52
53
54
55
56
57
58
59
60

roughly unchanged behavior over the 7−25×10^3 kW/cm^2 range, after which a slight decrease is noted, likely due to the saturation of the radiative recombination by excess generated carriers. However, at RT, the IQE increases rapidly with the increasing excitation energy density, due to the gradual saturation of the non-radiative recombination centers by generated carriers, reaching its maximum (76%) at ~ 8.2×10^3 kW/cm^2. This is followed by a decrease in the IQE at higher excitation energy densities, as shown in Figure 5a. The highest IQE value at 5 K is obtained at a lower excitation density than that at RT, due to the thermal activation of non-radiative recombination centers at RT.

Figure 5b shows the TRPL measurement values as a function of the carrier density. The aim of this analysis is to investigate the carrier dynamics and to understand the droop behavior inside the MQW only. The temporal evolution of the emission from the sample shows a bi-exponential decay, given by the following expression: [34]

$$I(t) = A_1\, exp\left(\frac{-t}{\tau_{PL1}}\right) + A_2\, exp\left(\frac{-t}{\tau_{PL2}}\right), \quad (4)$$

where A_1 and A_2 are adjustable constants and τ_{PL1} and τ_{PL2} are the fast and slow decay times, respectively. We observe that the fast decay is dominant in both the low and high temperature measurements as shown in Figure 5b. At 5 K, the PL lifetime initially increases with the increasing carrier generation rate, then starts to decrease when the rate reached 4×10^3 kW/cm^2. At RT, the PL lifetime shows a similar trend, albeit with a faster decay time. This decrease in the PL lifetime at 5 K and RT can be attributed to the growing predominance of radiative recombination. The excitation energy density increases at a higher carrier generation rate, indicating the high optical VLED quality and validating the results presented in Figure 4a. Therefore, the IQE droop observed at high-excitation carrier densities (Figure 5a) may be caused

1
2
3
4
5
6
7
8
9
10
11
12
13
14
15
16
17
18
19
20
21
22
23
24
25
26
27
28
29
30
31
32
33
34
35
36
37
38
39
40
41
42
43
44
45
46
47
48
49
50
51
52
53
54
55
56
57
58
59
60

by the saturation of radiative recombination in the MQW. The carrier density in the MQWs as a result of the saturation of the radiative recombination rate, while the subsequent increase in nonradiative recombination rate is due to the carrier leakage or electron overflow from the MQW, which eventually causes IQE droop with increasing carrier density, as shown in Figure 5(a).[35, 36]

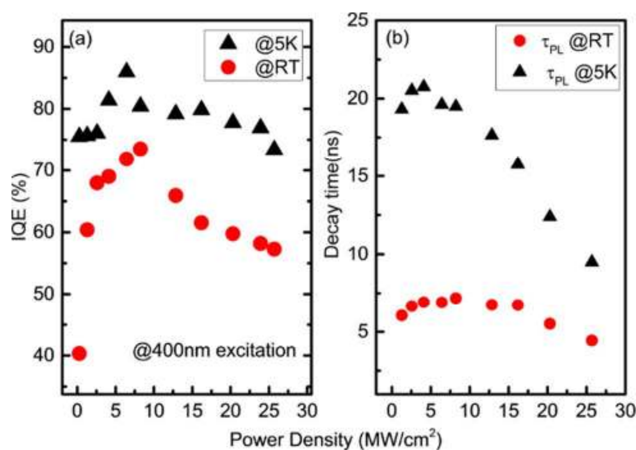

Figure 5. (a) Calculated IQE from the PDPL-integrated intensity at 5 K (black) and RT (red) as a function of excitation power density. (b) Carrier decay time inside the MQW obtained at different excitation power density values via the TRPL analysis.

CONCLUSION

The (-201)-oriented (β-Ga_2O_3) substrate is promising for the production of cost-effective, high-efficiency UV and visible InGaN/GaN MQW VLEDs that do not require complex processing techniques during fabrication. Its transparency and conductive properties are favorable for use in GaN-based high-efficiency VLEDs. Moreover, our conductive substrate exhibits an excellent vertical injection and n-side emitting geometry, promising better LEE compared to insulating substrates. The maximum IQE value obtained in our work exceeds 78%; the IQE initially increased with an increase in the injection current, due to an increase in

1
2
3
4
5
6
7
8
9
10
11
12
13
14
15
16
17
18
19
20
21
22
23
24
25
26
27
28
29
30
31
32
33
34
35
36
37
38
39
40
41
42
43
44
45
46
47
48
49
50
51
52
53
54
55
56
57
58
59
60

radiative recombination, and subsequently decreased once the band-filling effect became dominant. The PDPL and TRPL measurements showed that radiative recombination was dominant at higher carrier injection densities, with a negligible contribution from Auger recombination. Our results confirm that the (-201)-oriented (β-Ga_2O_3) is an ideal substrate for growing commercial VLEDs, as they can be produced using a straightforward, highly efficient, and direct growth process. The reliable performance of these VLEDs at RT, combined with their low cost, makes them suitable for applications where chip-size scalability is required.

ASSOCIATED CONTENT

Supporting Information

Derivation of fitting parameters of ABC rate equation for electroluminescence and photoluminescence excitations.

AUTHOR INFORMATION

Corresponding Author

*Email: iman.roqan@kaust.edu.sa

Notes

The authors declare no competing financial interest.

ACKNOWLEDGEMENT

The authors thank KAUST for the financial support.

REFERENCES

1. Jain, S. C.; Willander, M.; Narayan, J.; Overstraeten, R. V., III–nitrides: Growth, Characterization, and Properties. J. Appl. Phys. **2000**, 87, 965-1006.

2. Nakamura, S.; Pearton, S.; Fasol, G., The Blue Laser Diode: The Complete Story; Springer: Berlin, Heidelberg, **2013**; pp 1-28.

3. Schubert, E. F., Light-Emitting Diodes; Cambridge University Press **2006**; pp 1-26.

4. Ha, J. S.; Lee, S. W.; Lee, H. J.; Lee, H. J.; Lee, S. H.; Goto, H.; Kato, T.; Fujii, K.; Cho, M. W.; Yao, T., The Fabrication of Vertical Light-Emitting Diodes Using Chemical Lift-Off Process. IEEE Photonic. Tech. L. **2008**, 20, 175-177.

5. Kim, H.; Kim, K.-K.; Choi, K.-K.; Kim, H.; Song, J.-O.; Cho, J.; Baik, K. H.; Sone, C.; Park, Y.; Seong, T.-Y., Design of High-efficiency GaN-based Light Emitting Diodes with Vertical Injection Geometry. Appl. Phys. Lett. **2007**, 91, 023510.

6. Yang, Y. C.; Sheu, J. K.; Lee, M. L.; Tu, S. J.; Huang, F. W.; Lai, W. C.; Hon, S.; Ko, T. K., Vertical InGaN Light-emitting Diodes with a Sapphire-face-up Structure. Opt. Express **2012**, 20, A119-24.

7. Chen, W. H.; Kang, X. N.; Hu, X. D.; Lee, R.; Wang, Y. J.; Yu, T. J.; Yang, Z. J.; Zhang, G. Y.; Shan, L.; Liu, K. X.; Shan, X. D.; You, L. P.; Yu, D. P., Study of the Structural Damage in the (0001) GaN Epilayer Processed by Laser Lift-off Techniques. Appl. Phys. Lett. **2007**, 91, 121114.

8. Wu, Y. S.; Cheng, J.-H.; Peng, W. C.; Ouyang, H., Effects of Laser Sources on the Reverse-bias Leakages of Laser Lift-off GaN-based Light-emitting Diodes. Appl. Phys. Lett. **2007**, 90, 251110.

9. Schmitt, E.; Straubinger, T.; Rasp, M.; Weber, A.-D., Defect Reduction in Sublimation Grown SiC Bulk Crystals. Superlattice. Microst. **2006**, 40, 320-327.

10. Paskova, T.; Evans, K. R., GaN Substrates; Progress, Status, and Prospects. IEEE J. Sel. Top. Quant. **2009**, 15, 1041-1052.

11. Amilusik, M.; Sochacki, T.; Lucznik, B.; Fijalkowski, M.; Smalc-Koziorowska, J.; Weyher, J. L.; Teisseyre, H.; Sadovyi, B.; Bockowski, M.; Grzegory, I., Homoepitaxial HVPE-GaN Growth on Non-polar and Semi-polar Seeds. J. Cryst. Growth **2014**, 403, 48-54.

12. Víllora, E. G.; Shimamura, K.; Yoshikawa, Y.; Aoki, K.; Ichinose, N., Large-size β-Ga_2O_3 Single Crystals and Wafers. J. Cryst. Growth **2004**, 270, 420-426.

13. Galazka, Z.; Irmscher, K.; Uecker, R.; Bertram, R.; Pietsch, M.; Kwasniewski, A.; Naumann, M.; Schulz, T.; Schewski, R.; Klimm, D.; Bickermann, M., On the Bulk β-Ga_2O_3 Single Crystals Grown by the Czochralski Method. J. Cryst. Growth **2014**, 404, 184-191.

14. Muhammed, M. M.; Peres, M.; Yamashita, Y.; Morishima, Y.; Sato, S.; Franco, N.; Lorenz, K.; Kuramata, A.; Roqan, I. S., High Optical and Structural Quality of GaN Epilayers Grown on $(\bar{2}01)$ β-Ga_2O_3. Appl. Phys. Lett. **2014**, 105, 042112.

15. Muhammed, M. M.; Roldan, M. A.; Yamashita, Y.; Sahonta, S. L.; Ajia, I. A.; Iizuka, K.; Kuramata, A.; Humphreys, C. J.; Roqan, I. S., High-quality III-nitride Films on Conductive, Transparent $(\bar{2}01)$-oriented β-Ga_2O_3 Using a GaN Buffer Layer. Sci. Rep. **2016**, 6, 29747.

16 Liu, Z.; Yi, X.; Yu, Z.; Yuan, G.; Liu, Y.; Wang, J.; Li, J.; Lu, N.; Ferguson, I.; Zhang, Y., Impurity Resonant States p-type Doping in Wide-Band-Gap Nitrides. Sci. Rep. **2016**, 6, 19537.

17. Ju, I.; Kwon, Y.; Shin, C. S.; Kim, K. H.; Bae, S. J.; Kim, D. H.; Choi, J.; Ko, C. G., High-Power GaN-Based Light-Emitting Diodes Using Thermally Stable and Highly Reflective Nano-Scaled Ni–Ag–Ni–Au Mirror. IEEE Photonic. Tech. L. **2011**, 23, 1685-1687.

18 Chu, C.-F.; Lai, F.-I.; Chu, J.-T.; Yu, C.-C.; Lin, C.-F.; Kuo, H.-C.; Wang, S. C., Study of GaN Light-emitting Diodes Fabricated by Laser Lift-off Technique. J. Appl. Phys. **2004**, 95, 3916-3922.

19 Iizuka, K.; Morishima, Y.; Kuramata, A.; Shen, Y.-J.; Tsai, C.-Y.; Su, Y.-Y.; Liu, G.; Hsu, T.-C.; Yeh, J. H., InGaN LEDs Prepared on Beta-Ga_2O_3 (-201) Substrates. Proc. SPIE OPTO. **2015**, pp 93631Z-93631Z.

20. Shih, H.-Y.; Shiojiri, M.; Chen, C.-H.; Yu, S.-F.; Ko, C.-T.; Yang, J.-R.; Lin, R.-M.; Chen, M.-J., Ultralow Threading Dislocation Density in GaN Epilayer on Near-strain-free GaN Compliant Buffer Layer and its Applications in Hetero-epitaxial LEDs. Sci. Rep. **2015**, 5, 13671.

21. Ryu, H.-Y.; Choi, W. J., Optimization of InGaN/GaN Superlattice Structures for High-efficiency Vertical Blue Light-emitting Diodes. J. Appl. Phys. **2013**, 114, 173101.

22. Meneghini, M.; Trivellin, N.; Pavesi, M.; Manfredi, M.; Zehnder, U.; Hahn, B.; Meneghesso, G.; Zanoni, E., Leakage Current and Reverse-bias Luminescence in InGaN-based Light-emitting Diodes. Appl. Phys. Lett. **2009**, 95, 173507.

23. Xu, C.; Yu, T.; Yan, J.; Yang, Z.; Li, X.; Tao, Y.; Fu, X.; Chen, Z.; Zhang, G., Analyses of Light Extraction Efficiency in GaN-based LEDs Grown on Patterned Sapphire Substrates. Phys. Status solidi C **2012**, 9, 757-760.

24. Seong, T. Y.; Han, J.; Amano, H.; Morkoç, H., III-Nitride Based Light Emitting Diodes and Applications; Springer: Netherlands, **2014**; pp 162-175.

25. Dai, Q.; Shan, Q.; Cho, J.; Schubert, E. F.; Crawford, M. H.; Koleske, D. D.; Kim, M.-H.; Park, Y., On the Symmetry of Efficiency-versus-carrier-concentration Curves in GaInN/GaN

Light-emitting Diodes and Relation to Droop-causing Mechanisms. Appl. Phys. Lett. **2011**, 98, 033506.

26. Liu, Z.; Wei, T.; Guo, E.; Yi, X.; Wang, L.; Wang, J.; Wang, G.; Shi, Y.; Ferguson, I.; Li, J., Efficiency Droop in InGaN/GaN Multiple-quantum-well Blue Light-emitting Diodes Grown on Free-standing GaN Substrate. Appl. Phys. Lett. **2011**, 99, 091104.

27. Yoo, Y.-S.; Na, J.-H.; Son, S. J.; Cho, Y.-H., Effective Suppression of Efficiency Droop in GaN-based Light-emitting Diodes: Role of Significant Reduction of Carrier Density and Built-in Field. Sci. Rep. **2016**, 6, 34586.

28. Shim, J.-I.; Kim, H.; Han, D.-P.; Shin, D.-S.; Kim, K. S., Low Temperature Studies of the Efficiency Droop in InGaN-based Light-emitting Diodes. Proc. SPIE OPTO. **2014**, 8986, pp 89861S-89861S-8.

29. Yan, J.; Yu, T. J.; Li, X. B.; Tao, Y. B.; Xu, C. L.; Long, H.; Yang, Z. Y.; Zhang, G. Y., Efficiency Droop Behaviors of the Blue LEDs on Patterned Sapphire Substrate. J. Appl. Phys. **2011**, 110, 073102.

30. Ju, Z. G.; Tan, S. T.; Zhang, Z.-H.; Ji, Y.; Kyaw, Z.; Dikme, Y.; Sun, X. W.; Demir, H. V., On the Origin of the Redshift in the Emission Wavelength of InGaN/GaN Blue Light Emitting Diodes Grown with a Higher Temperature Interlayer. Appl. Phys. Lett. **2012**, 100, 123503.

31. Zheng, X. H.; Chen, H.; Yan, Z. B.; Li, D. S.; Yu, H. B.; Huang, Q.; Zhou, J. M., Influence of the Deposition Time of Barrier Layers on Optical and Structural Properties of High-efficiency Green-light-emitting InGaN⁄GaN Multiple Quantum Wells. J. Appl. Phys. **2004**, 96, 1899-1903.

32. Li, Q.; Xu, S. J.; Xie, M. H.; Tong, S. Y., Origin of the 'S-shaped' Temperature Dependence of Luminescent Peaks from Semiconductors. J. Phys-Condens Mat. **2005**, 17, 4853.

33. Takeda, K.; Mori, F.; Ogiso, Y.; Ichikawa, T.; Nonaka, K.; Iwaya, M.; Kamiyama, S.; Amano, H.; Akasaki, I., Internal Quantum Efficiency of GaN/AlGaN-based Multi Quantum Wells on Different Dislocation Densities Underlying Layers. Phys. Status solidi C **2010**, 7, 1916-1918.

34. Im, J. S.; Moritz, A.; Steuber, F.; Harle, V.; Scholz, F.; Hangleiter, A., Radiative Carrier Lifetime, Momentum Matrix Element, and Hole Effective Mass in GaN. Appl. Phys. Lett. **1997**, 70, 631-633.

35. Hammersley, S.; Watson-Parris, D.; Dawson, P.; Godfrey, M. J.; Badcock, T. J.; Kappers, M. J.; McAleese, C.; Oliver, R. A.; Humphreys, C. J., The Consequences of High Injected Carrier Densities on Carrier Localization and Efficiency Droop in InGaN/GaN Quantum Well Structures. J. Appl. Phys. **2012**, 111, 083512.

36. David, A.; Grundmann, M. J., Droop in InGaN Light-emitting Diodes: A Differential Carrier Lifetime Analysis. Appl. Phys. Lett. **2010**, 96, 103504.

1
2
3
4
5
6
7
8
9
10
11
12
13
14
15
16
17
18
19
20
21
22
23
24
25
26
27
28
29
30
31
32
33
34
35
36
37
38
39
40
41
42
43
44
45
46
47
48
49
50
51
52
53
54
55
56
57
58
59
60

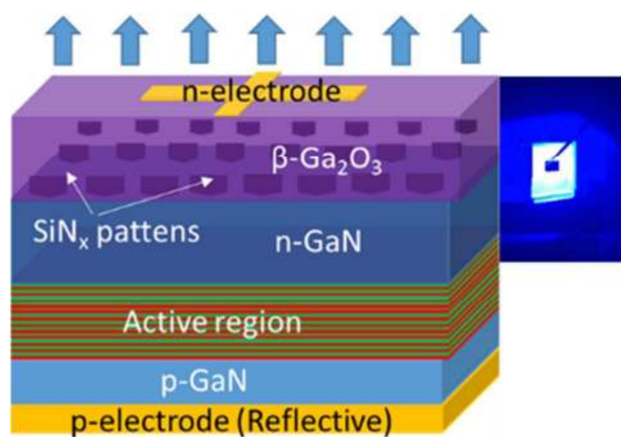

TOC

1
2
3
4
5
6
7
8
9
10
11
12
13
14
15
16
17
18
19
20
21
22
23
24
25
26
27
28
29
30
31
32
33
34
35
36
37
38
39
40
41
42
43
44
45
46
47
48
49
50
51
52
53
54
55
56
57
58
59
60

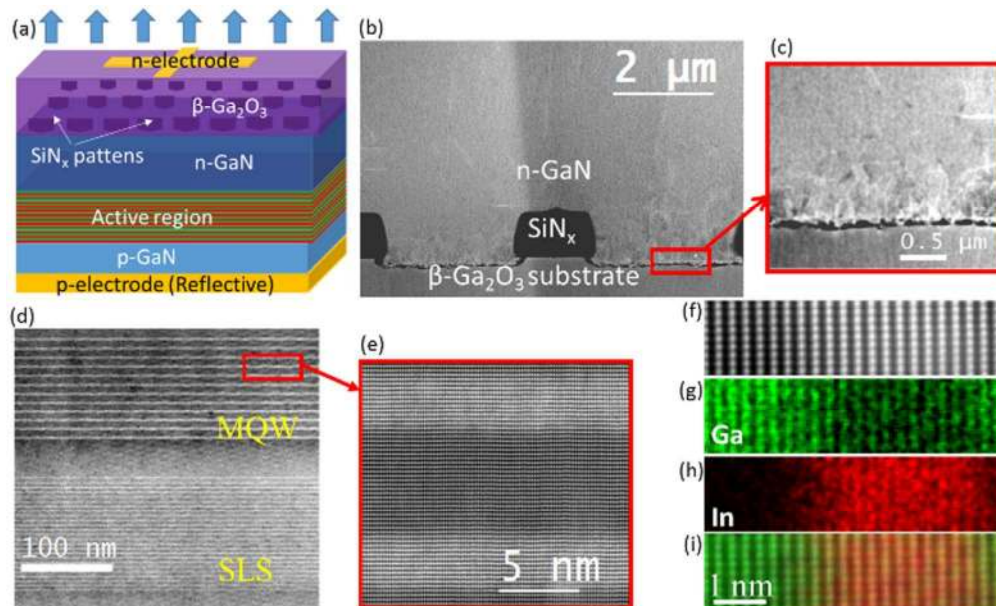

(a) The schematic structure of InGaN/GaN MQW VLED. (b) Cross-sectional STEM image of the interface between the substrate and VLED (The gap at the GaN/β-Ga_2O_3 interface was introduced during the TEM lamella preparation due to the easy cleavage planes of β-Ga_2O_3 substrate that can be damaged during preparation). (c) Enlarged image of the interface indicating the TD density. (d) STEM image of the InGaN/GaN SLS and MQW regions. (e) Atomic resolution STEM image of the QW and QB. (f) STEM image and corresponding EDX elemental map of Ga (g) and In (h), and (i) the superposition of Ga and In map with STEM image.

177x107mm (300 x 300 DPI)

1
2
3
4
5
6
7
8
9
10
11
12
13
14
15
16
17
18
19
20
21
22
23
24
25
26
27
28
29
30
31
32
33
34
35
36
37
38
39
40
41
42
43
44
45
46
47
48
49
50
51
52
53
54
55
56
57
58
59
60

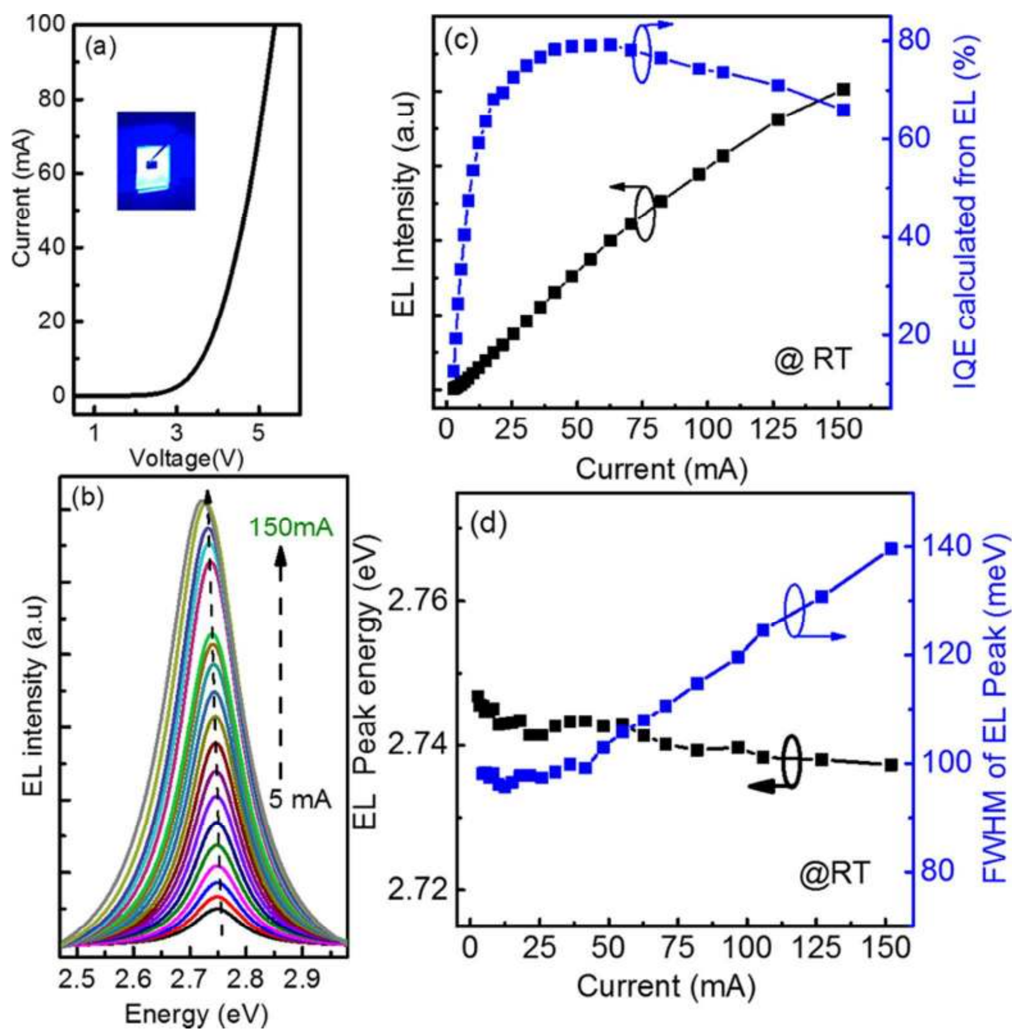

Figure 2. (a) I−V curve from InGaN/GaN MQWs VLED grown on β-Ga_2O_3 substrate (image of EL emission at an injection current of 20 mA is shown in the inset). (b) EL spectra as a function of the injection current in the VLED. (c) EL intensity and IQE as functions of the injection current for the VLED. (d) EL peak energy (black) and FWHM (blue) vs. the injection current.

82x83mm (300 x 300 DPI)

1
2
3
4
5
6
7
8
9
10
11
12
13
14
15
16
17
18
19
20
21
22
23
24
25
26
27
28
29
30
31
32
33
34
35
36
37
38
39
40
41
42
43
44
45
46
47
48
49
50
51
52
53
54
55
56
57
58
59
60

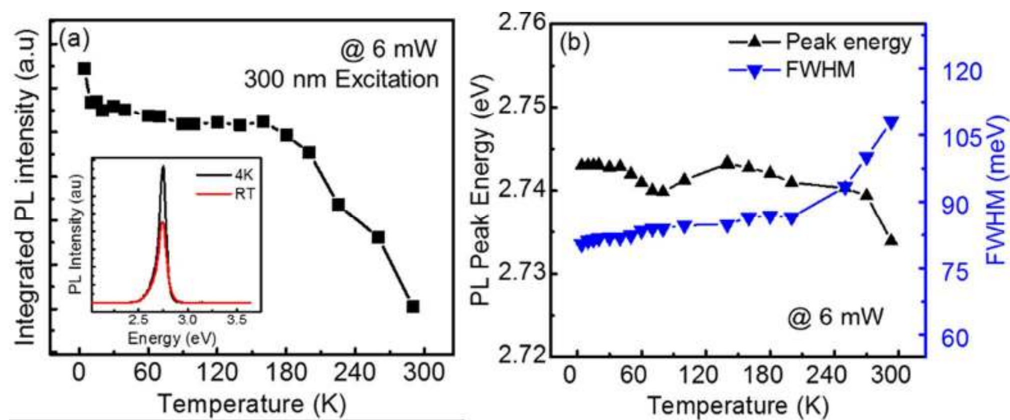

Figure 3. Temperature-dependent integrated PL analysis of the VLED structures under 325 nm laser excitation at 6 mW power. (a) Integrated PL intensity as a function of temperature increase (from 4 K to RT). The inset shows the PL spectra of the MQW peak at 5 K and RT (the ratio of the PL intensity at RT to that at 5 K is 72.5%). (b) PL peak position and FWHM of the MQW peak as a function of temperature.

84x34mm (300 x 300 DPI)

1
2
3
4
5
6
7
8
9
10
11
12
13
14
15
16
17
18
19
20
21
22
23
24
25
26
27
28
29
30
31
32
33
34
35
36
37
38
39
40
41
42
43
44
45
46
47
48
49
50
51
52
53
54
55
56
57
58
59
60

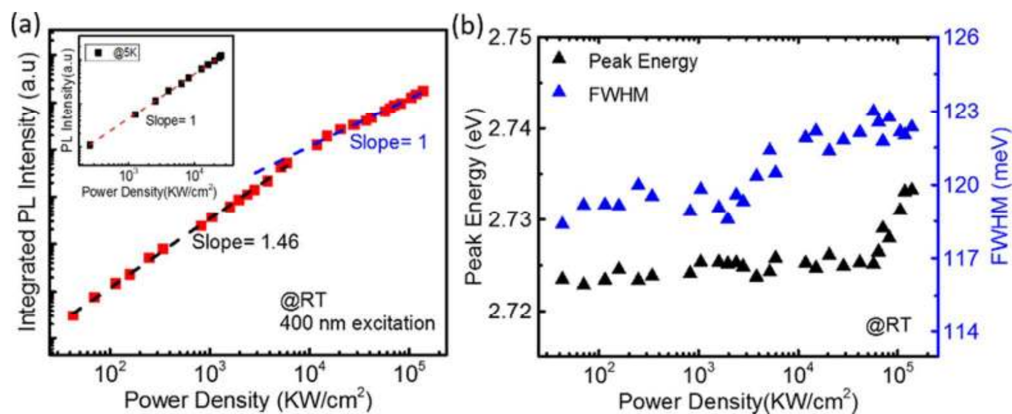

Figure 4. (a) Log-log plot of the integrated PL intensity output vs. the optically injected power density at RT. The values are fitted using two different slopes; the inset shows the same relationship at 5 K. (b) Analysis of the peak energy and FWHM of PDPL MQW emission spectra as a function of optically injected power density at RT.

82x33mm (300 x 300 DPI)

1
2
3
4
5
6
7
8
9
10
11
12
13
14
15
16
17
18
19
20
21
22
23
24
25
26
27
28
29
30
31
32
33
34
35
36
37
38
39
40
41
42
43
44
45
46
47
48
49
50
51
52
53
54
55
56
57
58
59
60

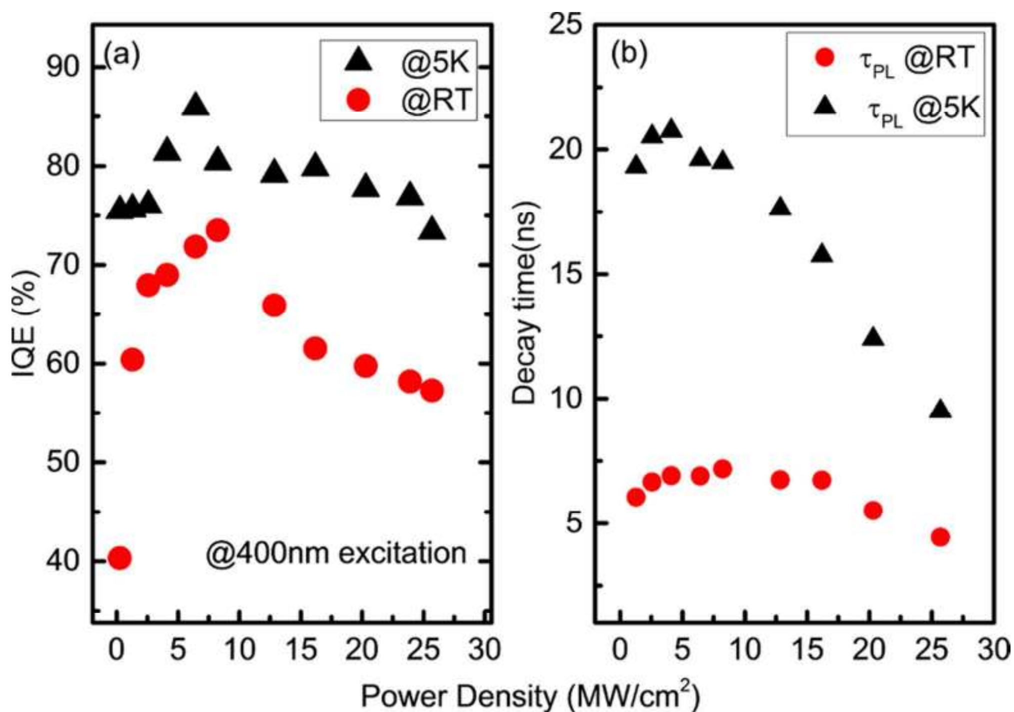

Figure 5. (a) Calculated IQE from the PDPL-integrated intensity at 5 K (black) and RT (red) as a function of excitation power density. (b) Carrier decay time inside the MQW obtained at different excitation power density values via the TRPL analysis.

82x57mm (300 x 300 DPI)

1
2
3
4
5
6
7
8
9
10
11
12
13
14
15
16
17
18
19
20
21
22
23
24
25
26
27
28
29
30
31
32
33
34
35
36
37
38
39
40
41
42
43
44
45
46
47
48
49
50
51
52
53
54
55
56
57
58
59
60

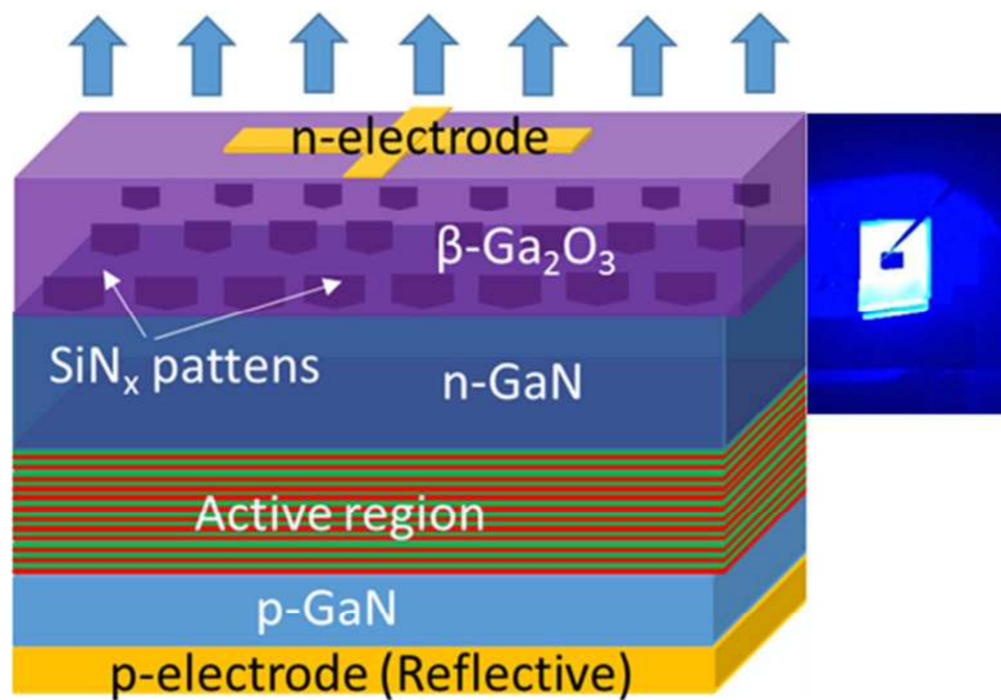

Table of Contents/Abstract Graphic

45x32mm (300 x 300 DPI)